# Geant4 X-ray fluorescence with updated libraries

Samer Bakr, David Cohen, Rainer Siegele, Jay Archer, Sebastien Incerti, Vladimir Ivanchenko, Alfonso Mantero, Anatoly Rosenfeld, Susanna Guatelli

# Geant4 X-ray fluorescence with updated libraries

Samer Bakr[a], David D. Cohen[b], Rainer Siegele[b], Jay W. Archer[a], Sebastien Incerti[c], Vladimir Ivanchenko[d,e], Alfonso Mantero[f], Anatoly Rosenfeld[a,g], Susanna Guatelli[a,g]

[a] Centre for Medical Radiation Physics, University of Wollongong, Wollongong, Australia

[b] Centre for Accelerator Science, Nuclear Science and Technology Organization, Menai, NSW, 2234, Australia

[c] Univ. Bordeaux, CNRS, CENBG, UMR 5797, F-33170 Gradignan, France

[d] Geant4 Associates International Ltd

[e] Tomsk State University, Tomsk, Russia

[f] SWHARD s.r.l.

[g] Illawarra Health and Medical Research Institute, University of Wollongong, Wollongong, Australia

## Abstract

We present the results concerning the development in Geant4 of a new data driven library, called here the ANSTO HF library. This X-ray fluorescence library is based on an approach of particular interest for PIXE simulation applications; however, it can be used in any Geant4 applications where X-ray fluorescence needs to be described. The X-ray fluorescence transition probabilities were calculated within the Hartree-Fock (HF) approach, which is recognised to better reproduce PIXE experimental values compared with the Hartree-Slater approach, adopted in the current default Geant4 EADL data library. These HF X-ray fluorescence transition probabilities were integrated into a new Geant4 library and will be released within Geant4 in the near future.

In this paper, we compare the fluorescence X-ray spectra generated by the ANSTO HF library and by the currently available library (EADL-1991 [1]) within Geant4, for targets irradiated with protons and $\alpha$ particles with energies up to 10 MeV, a range of interest for PIXE applications. The comparisons were performed for a large set of sample materials spanning a broad range of target atomic numbers. These two approaches were compared to existing experimental measurements performed at the ANSTO heavy ion microprobe beamline using 2 MeV and 3 MeV proton and 10 MeV $He^{2+}$ ion beams. This work represents a useful upgrade to the Geant4 atomic de-excitation package.

## Keywords

Geant4, PIXE, ionisation cross sections, X-ray fluorescence.

## Introduction

Particle Induced X-ray Emission (PIXE) is a well-established non-destructive analytical technique to determine the elemental composition of a sample, with very broad applications ranging from archaeometry to zoology.

PIXE describes the phenomenon of charged particles, such as protons, α and heavier ions, interacting with matter. This includes the ionisation of atoms within the target by removing one or more electrons from the K, L or M shells, followed by atomic de-excitation. This shell vacancy is then filled by an electron from an outer shell with the subsequent emission of a characteristic X-ray. These fluorescence X-rays are then detected and used to determine the elemental composition of the irradiated target. The elements in a sample are identified by the energy of the emitted X-rays while their concentration is determined by the intensity of each specific X-ray line [2].

Geant4 [3] is a general-purpose Monte Carlo toolkit, describing particle interactions in matter in the energy range from a few eV to TeV. In the context of PIXE, Geant4 allows one to model the composition of both homogeneous and heterogeneous materials, gaseous samples for environmental applications, planetary samples for geological and space science studies. Like the PIXAN and GUPIX [4] packages, Geant4 models PIXE taking into account the absorption of emitted X-rays and the slowing down of the incident particle as it passes through a target.

The Geant4 Atomic Relaxation package includes models for the generation of vacancies in atomic shells and the subsequent emission of fluorescence X-rays and Auger electrons. The development of the Geant4 Atomic Relaxation Package was firstly documented in [5] and was more recently improved [6]. Two concepts are considered in the simulation of atomic relaxation [5]: (1) the creation of a vacancy by a primary process and (2) the generation of the relaxation cascade. The first one is handled by any Geant4 Electromagnetic Physics Package (including Standard, Livermore, Penelope, and Geant4-DNA models) which manages the primary interactions, e.g., the photoelectric effect, Compton scattering and ionisation; the second one is handled by the Atomic Relaxation package, which is used by all the primary processes generating a vacancy. The secondaries generated by the Atomic Relaxation are then passed to Geant4 tracking and managed as any other particle in the simulation.

Different ionisation cross sections for protons and α particles can be currently used in Geant4 to generate the vacancy in a shell, as described in [7]: (1) K and L shell ionisation cross sections based on empirical and semi-empirical compilations [8]–[10]; (2) The so-called Form Factor set, based on an empirical polynomial approximation to the ionisation cross sections of K, L and a selection of M shells calculated from the ECPSSR theory for incident protons and α particles [11], [12]. (3) The third set, named ECPSSR Analytical, is based on the ECPSSR theory [13] for the description of K and L shells ionisation for incident protons and α particles [6]; (4) the fourth set, called ANSTO ECPSSR [14], based on the theoretical work of Brandt and Lapicki and documented in [15]–[18].

In addition, the Atomic Relaxation Geant4 component [5], [6], handling the emission of X-rays and Auger/Coster-Kronig electrons, is based on the Evaluated Data Library EADL [1], which provides the atomic electron binding energies and the radiative (fluorescence) and non-radiative (Auger and Coster–Kronig electrons) transition probabilities. Such tabulated data

are used to calculate the X-ray fluorescence lines [6] for Geant4 applications, where the modelling of atomic de-excitation is necessary. The radiative transition probabilities reported in the EADL were calculated according to Hartree-Slater (HS) methods [19], however following the work of Campbell et al. [20], [21] Cohen et al. [15] recommended the Hartree-Fock approach [22] rather than the Hartree-Slater model [19]. Validation studies of the G4-PIXE Package such as Guatelli et al. 2007 [5] and Pia et al. 2011 [23] showed that the EADL can reproduce the X-ray lines deriving from the K and L shell transitions within few percentage accuracy when compared to a selected experimental dataset by Deslattes et al. 2003 [24]. However, such agreement may be significantly improved by using data libraries based on Hartree-Fock method [15].

This project is motivated by the ongoing effort to improve the physics model as well as providing the user with a broader range of dataset options in Geant4 [6]. Despite the availability of different ionisation cross sections and atomic relaxation data sets, there is the need to provide a range of options as well as a unique, accurate, self-consistent and robust recommended approach to the PIXE user community, within Geant4. This improvement also benefits applications of Geant4 in other domains, such as environmental physics, geology, archaeology, and space science.

## Methods

The ECPSSR theory was developed by Brandt and Lapicki for both K and L subshell ionisation by light ions ($Z_1/Z_2$) < 0.3, where $Z_1$ and $Z_2$ refer to the charges of the projectile and the target atom, respectively [25]. Cohen and Harrigan published ECPSSR K and L subshell ionisation cross sections for both protons and α particles bombardment for ion energies in the general PIXE range from 0.2 to 10 MeV and for a wide variety of target atoms, from carbon to curium [16], [17]. Their later publication included corrections to this dataset for the relativistic nature of the ions. This correction was not large for the MeV ions used in PIXE with energies between 1 MeV to 3 MeV.

In Geant4, atomic relaxation simulation is articulated through two stages:

1) The creation of a vacancy by a primary process e.g., photoelectric effect, Compton scattering and ionisation. The shell (or subshell) where the vacancy is created by a process is sampled based on the cross section of the given process. For the ionisation process number and shell/sub-shell of the vacancies are calculated according to the PIXE cross sections. Two ionisation cross section models were used in this work:
    a. *ECPSSR Form Factor* [11], [12]: based on a polynomial approximation of the ionisation cross sections of K, L and a selection of M shells calculated with the ECPSSR theory for incident protons and α particles. This approach is the most recent available Geant4 set.
    b. *ANSTO ECPSSR* [14]: based on the ECPSSR approach of the ionisation cross sections of K, L and M sub/shells as calculated by D.D. Cohen et al. [15], [17] for incident protons and α particles. This approach was implemented in Geant4 and will be released in Geant4 within 2022.

2) The relaxation cascade is triggered, starting from the vacancy created by the primary process. Fluorescence X-ray, Auger electrons or Coster-Kronig transitions are generated through radiative and non-radiative transitions, based on the respective transition probabilities. In the simulation, all secondary particles with energies greater than the cut energy of 10 eV are tracked. Two transition probability libraries were used in this work to generate the fluorescence X-rays:
    a. *EADL* is the default library that is used in Geant4 to provide the transition probability and is based on Hartree-Slater approach [19].
    b. a new fluorescence data library, called here *ANSTO HF*, from ANSTO calculations based on Hartree-Fock approach [22]. This was written analogously to the existing EADL Geant4 data library, for simplicity, transparency and to facilitate its integration in the G4EMLOW data library. Same binding energies of EADL (as in G4EMLOW7.7) were adopted in the *ANSTO HF* library.

Table 1 lists the approaches used in this work.

*Table 1 models and approaches in this comparison*

| | **G4-default** | **G4-ANSTO** |
|---|---|---|
| **Ionisation cross sections** | *ECPSSR Form Factor* [11], [12] | *ANSTO ECPSSR* [14] |
| **Transition probabilities** | *EADL* (Hartree-Slater) [19] | *ANSTO HF* (Hartree-Fock) [22] |

Geant4 extended example *TestEm5* and Geant4 10.05.p01 were used. The impact of the two fluorescence libraries, *ANSTO HF* and *EADL*, was quantified in terms of fluorescence X-ray yields per incident particle. Nine target materials (Si, Ti, Fe, Zn, Nb, Ru, Ce, Ta, Au) were chosen, from low to high atomic number Z materials.

When the particle's velocity matches the electron shell velocity, the chance of the K electron shell ionisation is maximised. For example, protons and α particles when incident on silicon need a kinetic energy of ~3 MeV and ~25 MeV, respectively, to achieve some degree of velocity matching [26]. This is strongly dependent on the target atomic number *Z*. Monoenergetic pencil beams of protons (2 and 3 MeV) and α particles (10 MeV) were considered as they are representative of some common PIXE applications where experimental data may be available for comparison with theory. These particles were incident on 25 µm thick targets along the direction of the incident beam.

The production threshold of secondary particles was ignored. The fluorescence X-rays were counted once they were generated in the target. Note that the existing Geant4 PIXE *Empirical* and *Analytical* cross section sets [6] were not considered in this work as they generate only K and L vacancies.

Finally, the *G4-ANSTO* and *G4-default* (see Table 1) were compared to experimental measurements performed at ANSTO using the 6 MV SIRIUS Tandem Accelerator [27]. The experimental spectra were normalised to the highest line of the *G4-ANSTO* X-ray emissions.

### Experimental setup

PIXE spectra were experimentally measured at the ANSTO heavy ion microprobe beamline [27] using 2 and 3 MeV proton and 10 MeV $He^{2+}$ ion beams with beam currents varying between 0.5 and 2.5 nA. For X-ray detection, a 100 $mm^2$ high purity Ge detector with a solid angle of 90 msr was used. The detector has a 25 µm thick Be window. To prevent the scattered protons from entering the detector and to reduce the low energy X-ray yield from light elements such as the underlying Si in some of the samples, a 100 µm thick Mylar absorber (or filter) was placed in front of the detector. The data were collected using the Data Acquisition System mpsys4 from Melbourne University together with a Canberra Model 2060 digital signal processor. The irradiated samples were: 1 mm silicon layer, 100 nm Au layer on silicon, 50 nm TiN layer on silicon, 50 nm ZnO layer on silicon, 25 nm $Ta_2O_3$ layer on graphite, 25 nm Ru oxide film on graphite, 45 nm Nb oxide film on graphite, $Fe_2O_3$ layer embedded in a boron oxide pellet, and a sample of $CeO_2$ embedded in a boron oxide pellet.

## Results and discussion

The following figures (1, 2, 4, 5, 7, 8 and 10a) show the results of *G4-ANSTO* and *G4-default* approaches, with the X axis representing energy in keV and the Y axis representing X-ray frequency per incident particle. To compare *G4-ANSTO* to the experimental spectra, the *G4-ANSTO* data was convoluted with a Gaussian function. The reason behind calculating the Gaussian for *G4-ANSTO* is that there were different lines adjacent to each other and, therefore, their contribution was convoluted to produce the experimentally observed peaks.

In these figures (1, 2, 4, 5, 7, 8 and 10a), we simply calculated the Gaussian of *G4-ANSTO* and normalised it to the *G4-ANSTO* highest line to compare with the experimental data. Doing the same for the *G4-default* approach and plotting all the data and spectra on the same plot would deceive the readers and represent the Gaussian of both *G4-ANSTO* and *G4-default* to be nearly identical, as seen in figure (1).

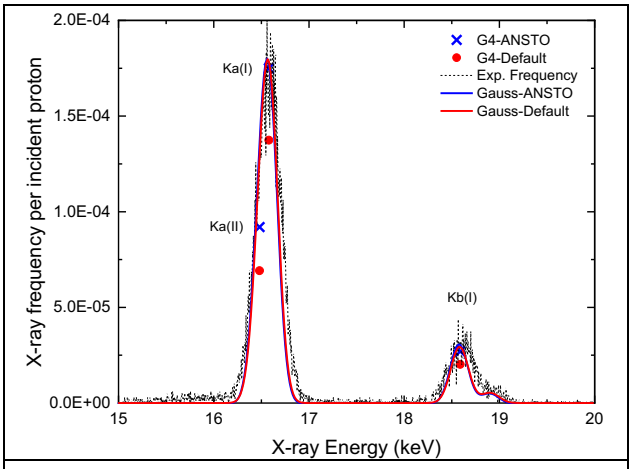


Fig. 1: X-ray emission generated by 2 MeV incident protons on a niobium target, Z=41.

Nonetheless, because the data libraries can be employed in a variety of applications ranging from space to environmental and healthcare applications, it is critical to demonstrate the absolute differences in X-ray emission yields produced with the two different data libraries.

**Comparison of 2 MeV incident protons results**

Figures 2, 3, and 4 compare the X-ray fluorescence yields obtained with *G4-default* and *G4-ANSTO* approaches, and experimental measurements. Figure 2 compares the X-ray emission frequencies (for the K shell) per incident particle generated by a 2 MeV proton on Si, Ti, Fe, Zn, Nb, and Ru samples. The Gaussian of *G4-ANSTO* results was calculated and compared with the experimental spectrum. The experimental spectra and the Gaussian of *G4-ANSTO* were normalised to the highest line of the *G4-ANSTO* X-ray emissions, in this case Kα(I). Figure 2 indicates that *G4-ANSTO* approach has higher X-ray emission rates (for Kα(I), Kα(II), and Kβ(I) X-ray lines) than the *G4-default* approach in all samples.

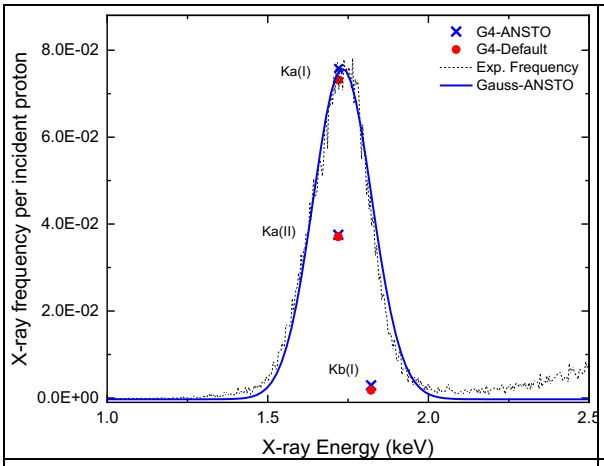


Fig. 2-a: X-ray emission generated by 2 MeV incident protons on a silicon target, Z=14.

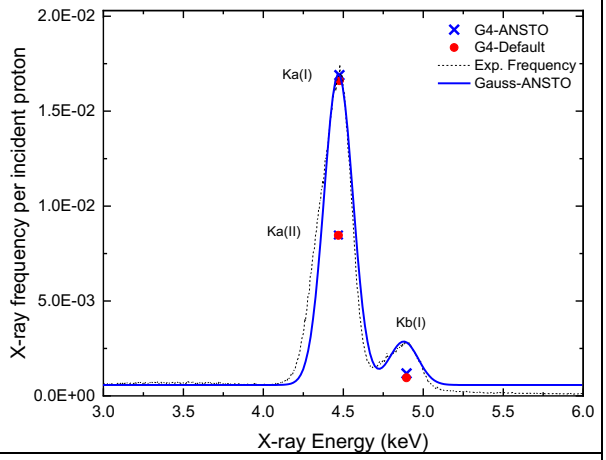


Fig. 2-b: X-ray emission generated by 2 MeV incident protons on a titanium target, Z=22.

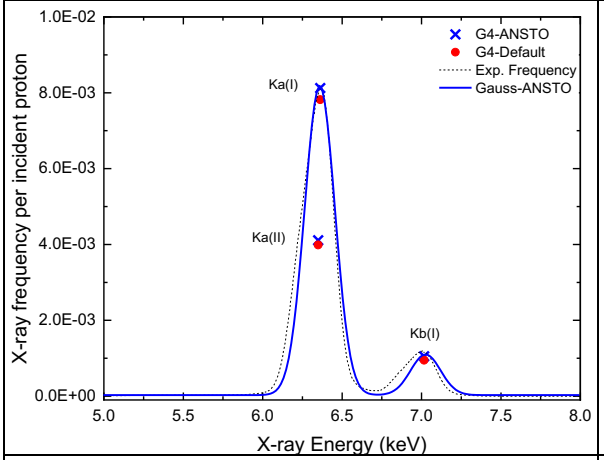


Fig. 2-c: X-ray emission generated by 2 MeV incident protons on an iron target, Z=26.

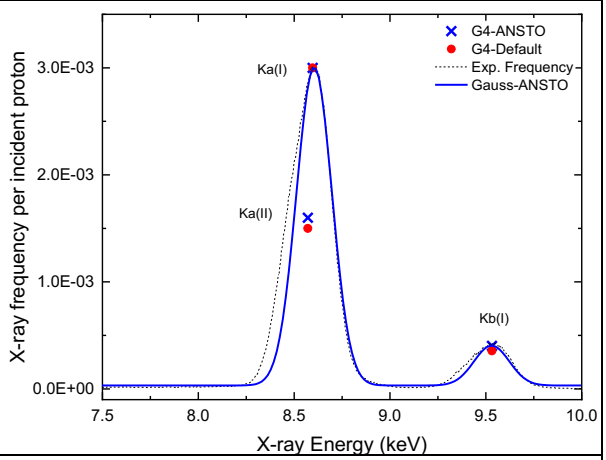


Fig. 2-d: X-ray emission generated by 2 MeV incident protons on a zinc target, Z=30.

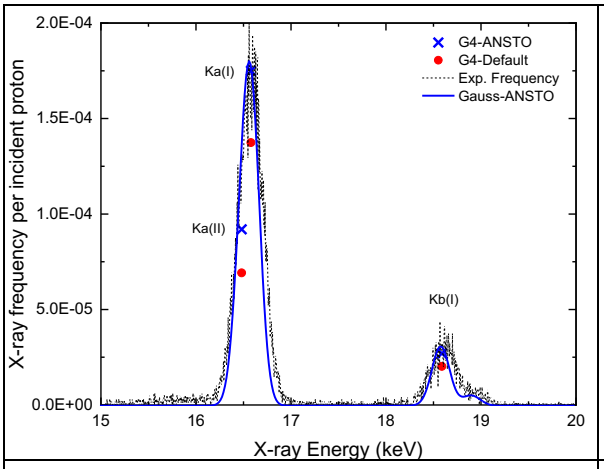


Fig. 2-e: X-ray emission generated by 2 MeV incident protons on a niobium target, Z=41.

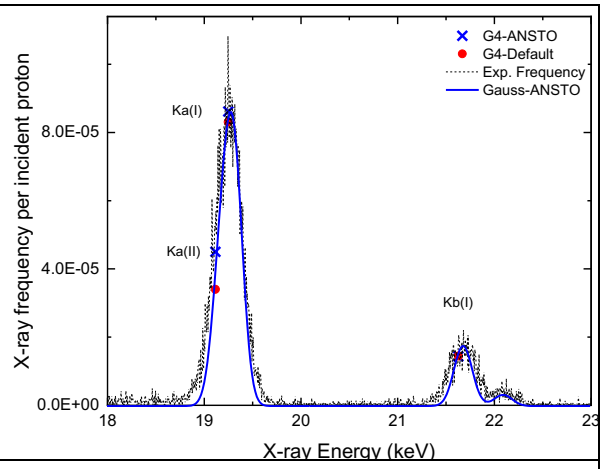


Fig. 2-f: X-ray emission generated by 2 MeV incident protons on a ruthenium target, Z=44.

192

193 The ratio of *G4-ANSTO* to *G4-default* calculated X-ray yields of Nb and Ru derived primarily
194 from vacancies in the K and L shells produced by incident 2 MeV protons is shown in figure 3.

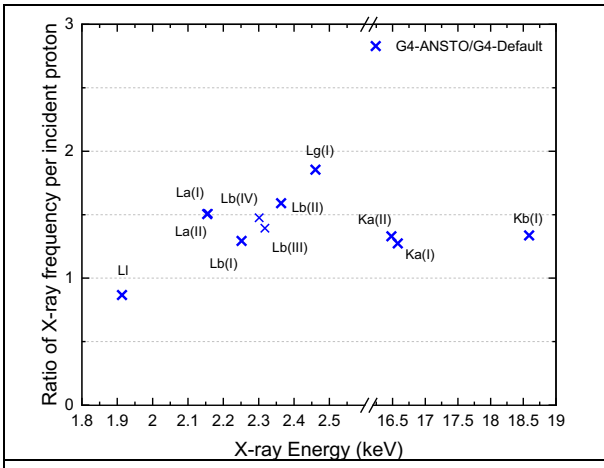


Fig. 3-a: Ratio of X-ray emission generated by 2 MeV incident protons on a niobium target, Z=41.

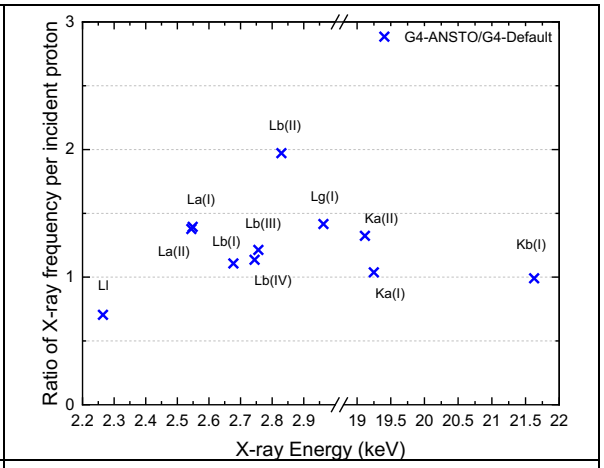


Fig. 3-b: Ratio of X-ray emission generated by 2 MeV incident protons on a ruthenium target, Z=44.

195

196 Figure 4 compares calculated X-ray yields to experimental spectra of Ce and Ta, which are
197 driven primarily by vacancies in the L shell created by incident 2 MeV protons.

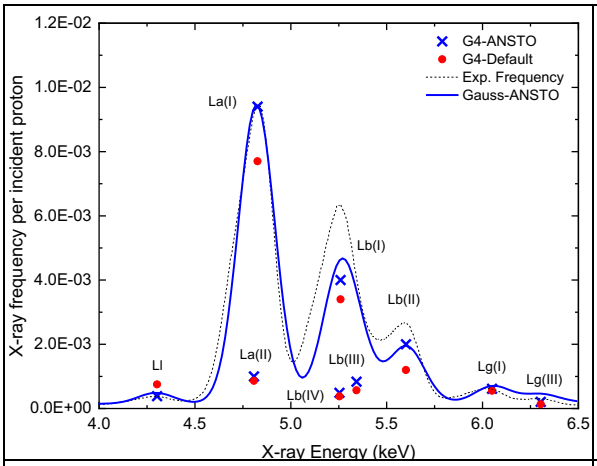


Fig. 4-a: X-ray emission generated by 2 MeV incident protons on a cerium target, Z=58.

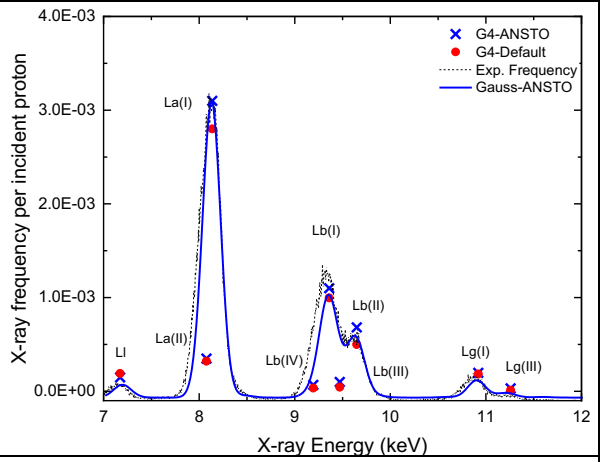


Fig. 4-b: X-ray emission generated by 2 MeV incident protons on a tantalum target, Z=73.

The L shell X-ray emissions for Nb (Z=41) and Ru (Z=44) samples were not obtained experimentally. Therefore, only the results of Geant4 simulation using the *G4-ANSTO* and *G4-default* approaches are shown in figure 3. The ratio of the lines generated by *G4-ANSTO* approach to the *G4-default* approach was displayed in figure 3. Most of Geant4 lines were found to be substantially higher in the *G4-ANSTO* approach for both samples (Nb and Ru). It can be noticed that most lines show no more ~50% difference between *G4-ANSTO* and *G4-default* approaches, while it is around ~100% difference for Lγ(I) and Lβ(II) for Nb and Ru, respectively. Except the Ll line, the electron transition from M(I) subshell to L(III) subshell, in *G4-ANSTO* results is about ~25% lower than in *G4-default* results.

Figure 4 depicts the findings, which indicate a reasonable agreement between Geant4-calculated emission X-ray spectra and the experimental measurements. We found that the *G4-ANSTO* approach produces higher X-ray emission results than the *G4-default* one. The difference was particularly noticeable for the Lα(I) line. In addition, the lines (Lβ (I), (II), (III), (IV)) calculated by means of both *G4-ANSTO* and *G4-default* approaches were lower than the experimental spectrum, which was attributable to the fact that these four lines were adjacent to each other and, therefore, their contribution was convoluted to produce the higher peaks observable in the experimental data. However, the Gaussian spectra of *G4-ANSTO* approach showed better results when compared to the experimental spectrum.

As shown in figure 4, the Ll line of cerium produced by the *G4-default* approach was higher than that generated by the *G4-ANSTO* one. The X-ray fluorescence databases of *G4-default* and *G4-ANSTO* approaches were compared to understand the reason for these variations in Ll X-ray yield and it was found that only the Ll X-ray line probability of transition was higher in *G4-default* when compared to *G4-ANSTO*.

**Comparison of 3 MeV incident protons results**

Figure 5 compares calculated X-ray yields to experimental spectra of Si, Ti, Fe, Zn, Nb, and Ru derived primarily from vacancies in the K shell induced by incident 3 MeV protons.

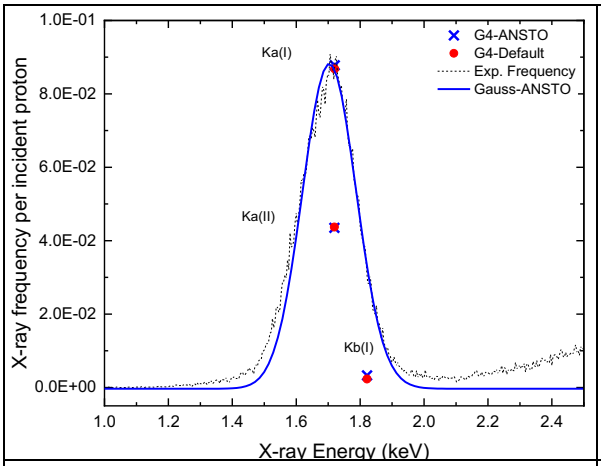


Fig. 5-a: X-ray emission generated by 3 MeV incident protons on a silicon target, Z=14.

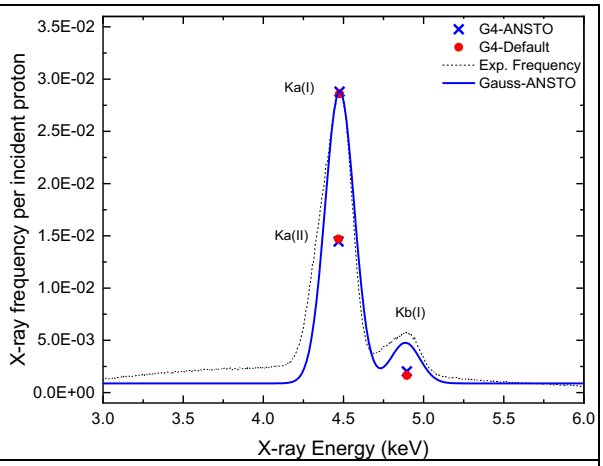


Fig. 5-b: X-ray emission generated by 3 MeV incident protons on a titanium target, Z=22.

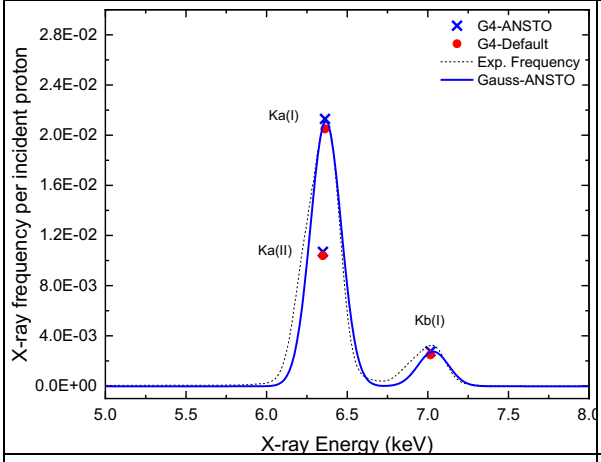


Fig. 5-c: X-ray emission generated by 3 MeV incident protons on an iron target, Z=26.

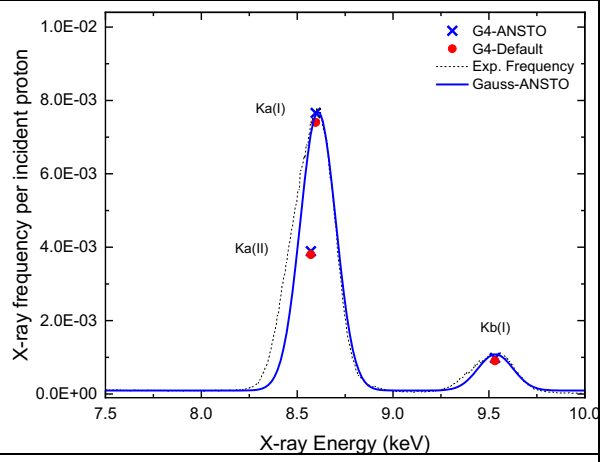


Fig. 5-d: X-ray emission generated by 3 MeV incident protons on a zinc target, Z=30.

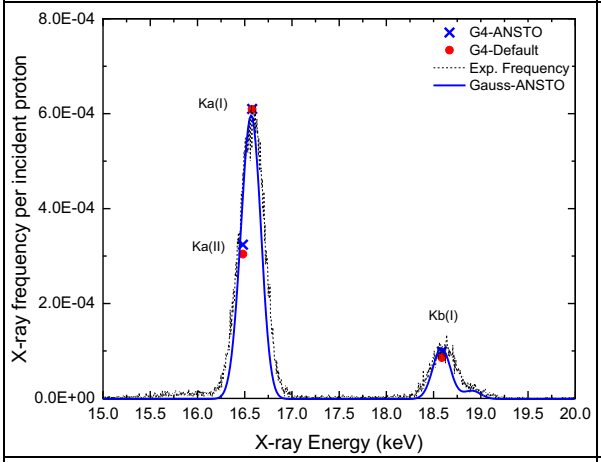


Fig. 5-e: X-ray emission generated by 3 MeV incident protons on a niobium target, Z=41.

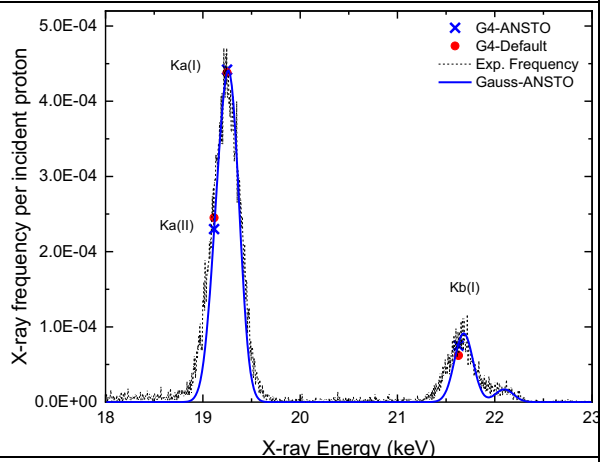


Fig. 5-f: X-ray emission generated by 3 MeV incident protons on a ruthenium target, Z=44.

225

Figure 6 depicts the measured X-ray yields of Nb and Ru, which were primarily derived from vacancies in the L and K shells induced by incident 3 MeV protons.

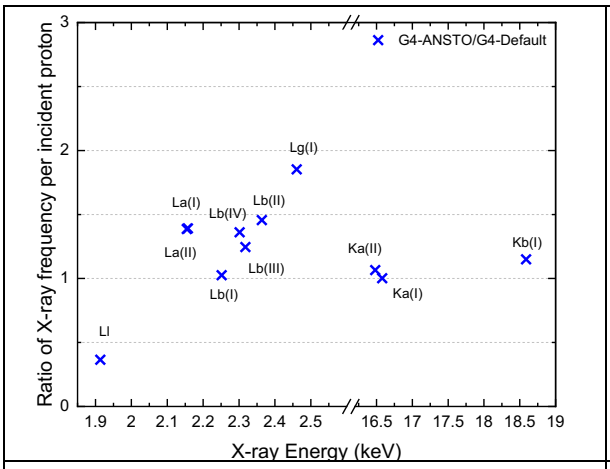


Fig. 6-a: Ratio of X-ray emission generated by 3 MeV incident protons on a niobium target, Z=41.

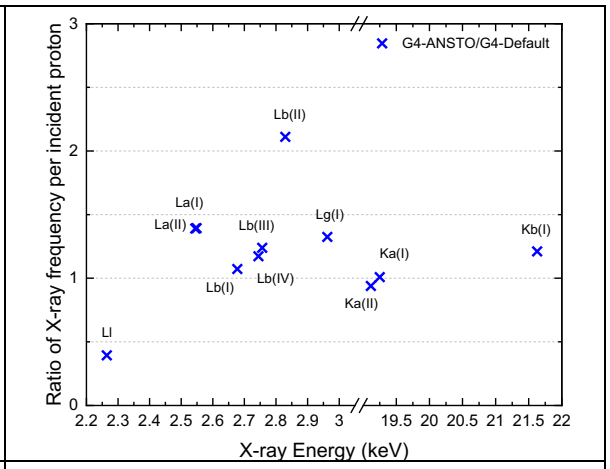


Fig. 6-b: Ratio of X-ray emission generated by 3 MeV incident protons on a ruthenium target, Z=44.

Figure 7 compares calculated X-ray yields to experimental spectra of Ce, Ta, and Au, which were driven primarily by vacancies in the L shell induced by incident 3 MeV protons.

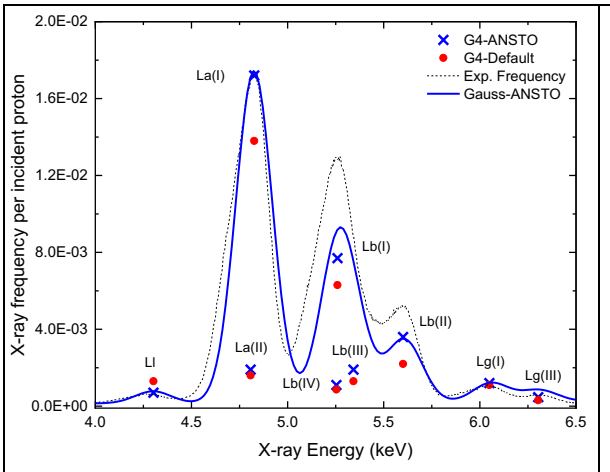


Fig. 7-a: X-ray emission generated by 3 MeV incident protons on a cerium target, Z=58.

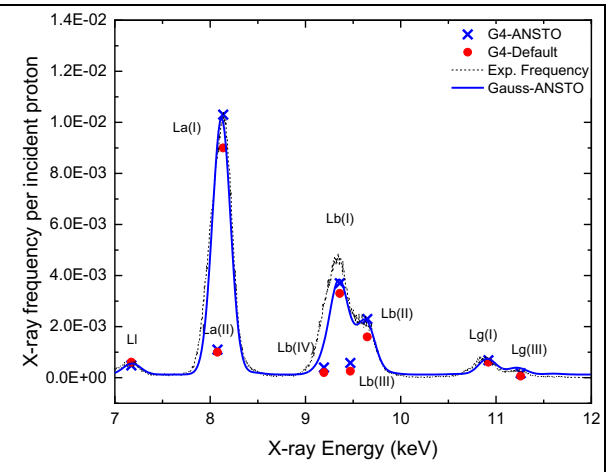


Fig. 7-b: X-ray emission generated by 3 MeV incident protons on a tantalum target, Z=73.

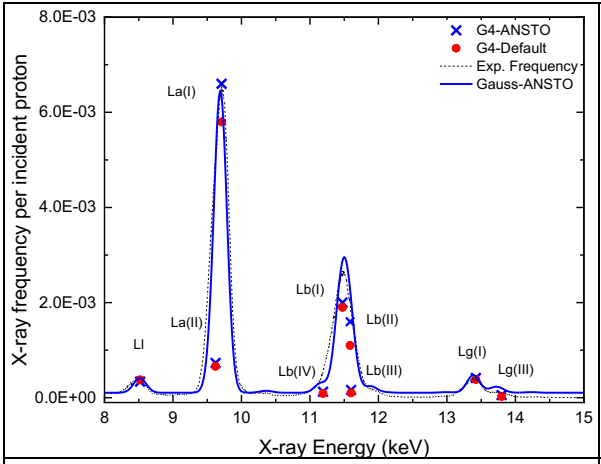


Fig. 7-c: X-ray emission generated by 3 MeV incident protons on a gold target, Z=79.

Figures 5, 6, and 7 provide a comparison of the *G4-ANSTO* and *G4-default* approaches' results. Figure 5 compares the calculated *G4-ANSTO* and *G4-default* X-ray emission frequencies (for the K shell) per incident particle, produced by a 3 MeV proton on Si, Ti, Fe, Zn, Nb, and Ru samples to experimental measurements. Additionally, the experimental spectrum was compared to the Gaussian of *G4-ANSTO* results. The experimental spectra and the Gaussian of *G4-ANSTO* were normalised to the highest line of the *G4-ANSTO* X-ray emissions, in this case Kα(I). Figure 5 shows that the *G4-ANSTO* approach provides higher X-ray emission frequencies than the *G4-default* approach in all samples, except for Kα(II) X-ray line for Ru (see figure 5-f).

Since the L shell experimental spectra for these samples are not available, figure 6 only shows the results of the Geant4 simulation, the ratio of lines generated by the *G4-ANSTO* approach to lines generated by the *G4-default* approach. It is worth noting that all lines show less than ~50% difference between *G4-ANSTO* and *G4-default* approaches, while Lγ(I) and Lβ(II) for Nb and Ru, respectively, show about ~100% difference.

Figure 7 indicates that the Gaussian of *G4-ANSTO* emission X-ray spectra and the experimental measurements agreed reasonably well. The experimental spectrum and the Gaussian of *G4-ANSTO* were normalised to the highest line of the *G4-ANSTO* approach. We found that the *G4-ANSTO* approach produces higher X-ray emission results than the *G4-default* results. The differentiation was especially evident in the Lα(I) line.

Figures 6 and 7 show that only the Ll X-ray yield is about ~60% higher in *G4-default* approach than in *G4-ANSTO* one since the probability of transition for the Ll X-ray line was higher in *G4-default* approach.

**Comparison of 10 MeV incident α particles results**

Figure 8 compares calculated X-ray yields to experimental spectra of Ti, Zn, Nb, and Ru derived primarily from vacancies in the K shell induced by incident 10 MeV α particles.

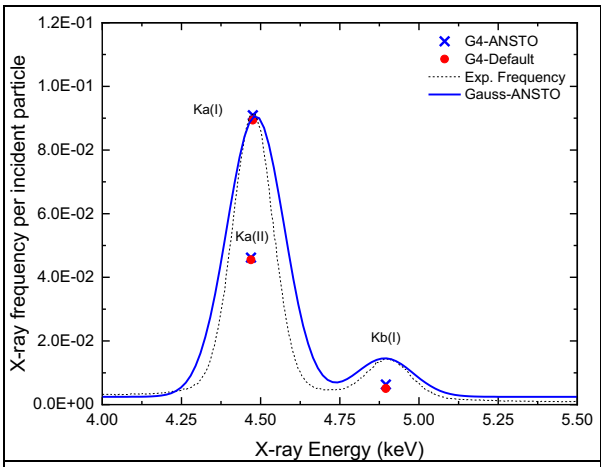


Fig. 8-a: X-ray emission generated by 10 MeV incident α particles on a titanium target, Z=22.

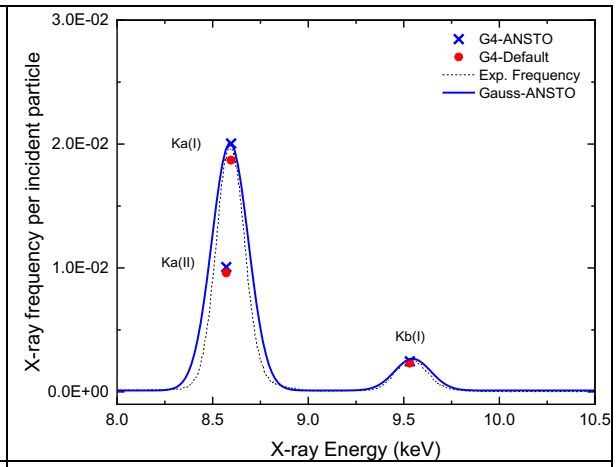


Fig. 8-b: X-ray emission generated by 10 MeV incident α particles on a zinc target, Z=30.

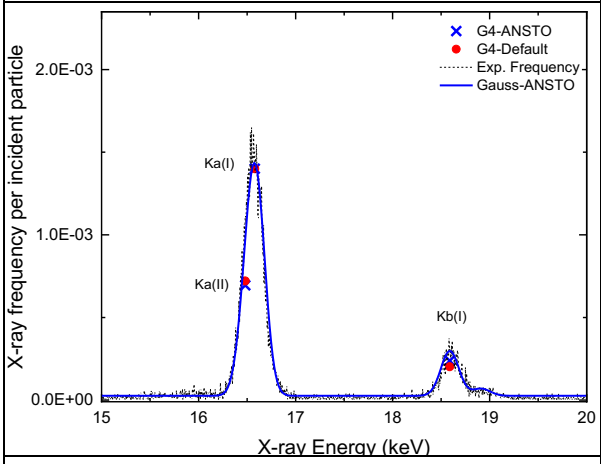


Fig. 8-c: X-ray emission generated by 10 MeV incident α particles on a niobium target, Z=41.

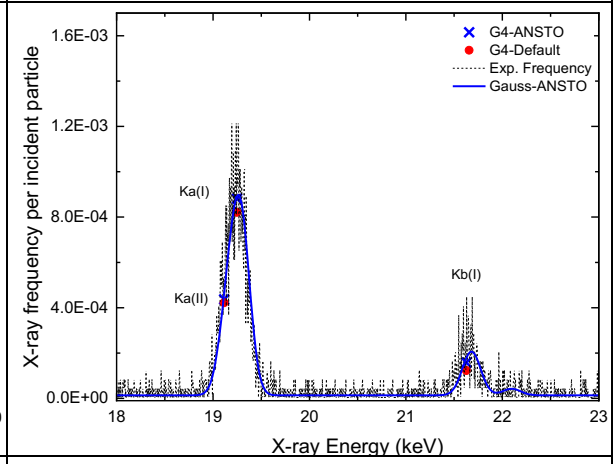


Fig. 8-d: X-ray emission generated by 10 MeV incident α particles on a ruthenium target, Z=44.

Figure 9 depicts the calculated X-ray yields of Nb and Ru, which result primarily from vacancies in the L and K shells induced by incident 10 MeV α particles.

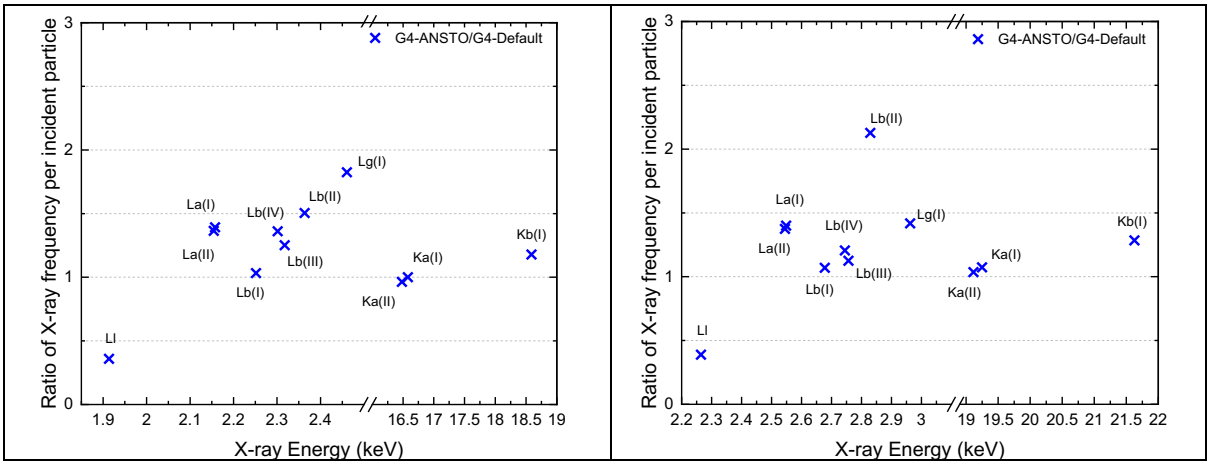

| Fig. 9-a Ratio of X-ray emission generated by 10 MeV incident α particles on a niobium target, Z=41. | Fig. 9-a Ratio of X-ray emission generated by 10 MeV incident α particles on a ruthenium target, Z=44. |
|---|---|

Figure 10 compares calculated X-ray yields to experimental Ta spectra derived primarily from vacancies in the L shell induced by 10 MeV incident α particles.

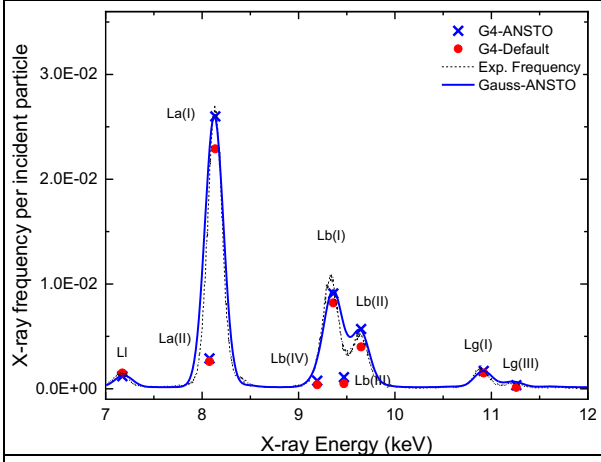


Fig. 10-a: X-ray emission generated by 10 MeV incident α particles on a tantalum target, Z=73.

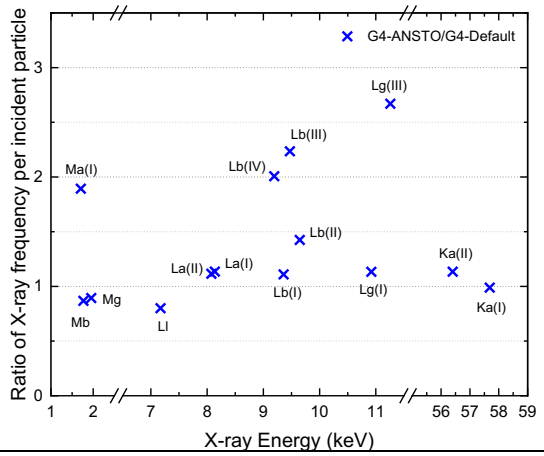


Fig. 10-b: X-ray emission generated by 10 MeV incident α particles on a tantalum target, Z=73.

Figures 8, 9, and 10 compare the results of the *G4-ANSTO* and *G4-defaul*t approaches. Figure 8 compares the X-ray emission frequencies (for the K shell), produced by 10 MeV α particles on Ti, Zn, Nb, and Ru samples, calculated using the *G4-ANSTO* and *G4-default* approaches to experimental measurements. The Gaussian of *G4-ANSTO* results were compared to the experimental spectrum. The experimental spectra and the Gaussian of *G4-ANSTO* were normalised to the highest line of *G4-ANSTO* approach, in this case Kα(I). Figure 8 shows that the *G4-ANSTO* approach indicates about ~5% higher X-ray emission frequencies than the *G4-default* approach in all samples. Figure 9 depicts the L and K shells X-ray emissions using the *G4-ANSTO* and *G4-default* approaches; the *G4-ANSTO* results were significantly higher than the *G4-default* results, a maximum of 50% difference for most lines, while Lγ(I) and Lβ(II) for Nb and Ru, respectively, showed about ~100% difference. Besides the Ll line, which was ~60% lower using *G4-ANSTO* approach than *G4-default* approach.

Figure 10 depicts the calculated Ta X-ray yields resulting primarily from vacancies in the L and M shells induced by 10 MeV incident α particles. In Figure 10-a, the Gaussian of *G4-ANSTO* X-ray emission results showed a reasonably good agreement with the ANSTO experimental data. Figure 10-b, on the other hand, depicts the M and L shells X-ray emissions for both the *G4-ANSTO* and *G4-default* approaches under consideration. Except for the Ll X-ray line, all *G4-ANSTO* X-ray lines created from vacancies in L shells were higher (maximum of 100% besides of Lβ(III) and Lγ(III) are about 150% higher) than the *G4-default* ones, due to the higher probability of transition in the *G4-default* approach, with the solely exception of the Mβ and Mγ X-ray lines.

## Conclusions

The *G4-ANSTO* approach, which includes the *ANSTO ECPSSR* ionisation cross sections [14] and *ANSTO HF* fluorescence yield [22] libraries, was implemented in Geant4 and compared to *G4-default* approach. The *G4-default* approach includes the *ECPSSR Form Factor* ionisation cross sections [11], [12] and *EADL* [19] fluorescence yield libraries. Geant4-calculated X-ray emission spectra using the *G4-ANSTO,* and the *G4-default* approaches were compared in terms of fluorescence X-ray yields per incident particle. Nine target materials (Si, Ti, Fe, Zn, Nb, Ru, Ce, Ta, Au) were under study, from low to high atomic number Z materials. Monoenergetic beams of protons (2 and 3 MeV) and α particles (10 MeV) were used.

For all samples, most lines were observed to be significantly higher when using the *G4-ANSTO* approach with the exception of the Ll line, corresponding to the electron transition from the M(I) subshell to the L(III) subshell. The study showed that the Geant4-calculated X-ray emission spectra and the ANSTO experimental measurements were in a reasonably good agreement. However, we are only analysing a few peaks with PIXE, but in reality, *G4-ANSTO* has significant differences with *G4-default* for other lines, which may be important in other application domains.

The novel *G4-ANSTO* X-ray fluorescence data libraries can be coupled with the G4-ANSTO cross sections [14] or with the Geant4 default cross sections, handling the generation of atomic vacancies (e.g., the photoelectric effect, Compton scattering and ionisation).

The *G4-ANSTO* approach will be included in the public release of Geant4 in the near future and will be usable by means of user interface commands on top of any electromagnetic physics configurations. The Geant4 PIXE user community will be able to use the *G4-ANSTO* libraries and models, which provide a unique, self-consistent, and stable recommended approach.

## Acknowledgment

This work was funded by the Australian Research Council, grant number ARC DP 170100967. The authors would like to acknowledge the Australian National Collaborative Research Infrastructure Scheme (NCRIS) funding for accelerators and Centre for Accelerator Science staff for access to their ion beam analysis facilities.

## References

[1] S. T. Perkins, D. E. Cullen, M. H. Chen, J. Rathkopf, J. Scofield, and J. H. Hubbell, “Tables and Graphs of Atomic Subshell and Relaxation Data Derived from the LLNL Evaluated Atomic Data Library, ${Z}=1-100$,” *Eadl*, vol. 30, p. UCRL-50400, 1991.

[2] H. R. Verma, “X-ray fluorescence (XRF) and particle-induced X-ray emission (PIXE),” *At. Nucl. Anal. Methods XRF, Mössbauer, XPS, NAA B63Ion-Beam Spectrosc. Tech.*, pp. 1–90, 2007.

[3] S. Agostinelli *et al.*, “Geant4—a simulation toolkit,” *Nucl. Instruments Methods Phys. Res. Sect. A Accel. Spectrometers, Detect. Assoc. Equip.*, vol. 506, no. 3, pp. 250–303,

2003.

[4] E. Clayton, P. Duerden, and D. D. Cohen, “A discussion of PIXAN and PIXANPC: The AAEC PIXE analysis computer packages,” *Nucl. Inst. Methods Phys. Res. B*, vol. 22, no. 1–3, pp. 64–67, Mar. 1987.

[5] S. Guatelli, A. Mantero, B. Mascialino, P. Nieminen, and M. G. Pia, “Geant4 Atomic Relaxation,” *IEEE Trans. Nucl. Sci.*, vol. 54, no. 3, pp. 585–593, 2007.

[6] A. Mantero *et al.*, “PIXE simulation in Geant4,” *X-Ray Spectrom.*, vol. 40, no. 3, pp. 135–140, 2011.

[7] S. Incerti *et al.*, “Comparison of experimental proton-induced fluorescence spectra for a selection of thin high-Z samples with Geant4 Monte Carlo simulations,” *Nucl. Instruments Methods Phys. Res. Sect. B Beam Interact. with Mater. Atoms*, vol. 358, pp. 210–222, 2015.

[8] H. Paul and J. Sacher, “Fitted empirical reference cross sections for K-shell ionization by protons,” *At. Data Nucl. Data Tables*, vol. 42, no. 1, pp. 105–156, 1989.

[9] H. Paul and O. Bolik, “Fitted empirical reference cross sections for K-shell ionization by alpha particles,” *At. data Nucl. data tables*, vol. 54, no. 1, pp. 75–131, 1993.

[10] I. Orlic, C. H. Sow, and S. M. Tang, “Experimental L-shell X-ray production and ionization cross sections for proton impact,” *At. data Nucl. data tables*, vol. 56, no. 1, pp. 159–210, 1994.

[11] A. Taborda, P. C. Chaves, and M. A. Reis, “Polynomial approximation to universal ionisation cross-sections of K and L shells induced by H and He ion beams,” *X-Ray Spectrom.*, vol. 40, no. 3, pp. 127–134, 2011.

[12] A. Taborda, P. C. Chaves, M. L. Carvalho, and M. A. Reis, “Polynomial approximation to universal M-shell ionisation cross-sections induced by H+ and He2+ ions,” *X-Ray Spectrom.*, vol. 42, no. 4, pp. 177–182, 2013.

[13] H. Ben Abdelouahed, S. Incerti, and A. Mantero, “New Geant4 cross section models for PIXE simulation,” *Nucl. Instruments Methods Phys. Res. Sect. B Beam Interact. with Mater. Atoms*, vol. 267, no. 1, pp. 37–44, 2009.

[14] S. Bakr *et al.*, “Latest Geant4 developments for PIXE applications,” *Nucl. Instruments Methods Phys. Res. Sect. B Beam Interact. with Mater. Atoms*, vol. 436, no. October, pp. 285–291, 2018.

[15] D. D. Cohen, J. Crawford, and R. Siegele, “K, L, and M shell datasets for PIXE spectrum fitting and analysis,” *Nucl. Instruments Methods Phys. Res. Sect. B Beam Interact. with Mater. Atoms*, vol. 363, pp. 7–18, 2015.

[16] D. D. Cohen and M. Harrigan, “K- and L-shell ionization cross sections for protons and helium ions calculated in the ecpssr theory,” *At. Data Nucl. Data Tables*, vol. 33, no. 2,

pp. 255–343, 1985.

[17] D. D. Cohen and M. Harrigan, “L shell line intensities for light ion induced X-ray emission,” *Nucl. Instruments Methods Phys. Res. Sect. B Beam Interact. with Mater. Atoms*, vol. 15, no. 1, pp. 576–580, 1986.

[18] D. D. Cohen, “K- and L-shell ionization cross sections for deuterons calculated in the ECPSSR theory,” *At. Data Nucl. Data Tables*, vol. 41, no. 2, pp. 287–338, 1989.

[19] D. L. Walters and C. P. Bhalla, “Z dependence of the K-LL auger rates,” *Phys. Rev. A*, vol. 3, no. 1, pp. 519–520, 1971.

[20] J. L. Campbell, “Fluorescence yields and Coster-Kronig probabilities for the atomic L subshells,” *At. Data Nucl. Data Tables*, vol. 85, no. 2, pp. 291–315, 2003.

[21] J. L. Campbell, “Fluorescence yields and Coster-Kronig probabilities for the atomic L subshells. Part II: The L1 subshell revisited,” *At. Data Nucl. Data Tables*, vol. 95, no. 1, pp. 115–124, 2009.

[22] J. H. Scofield, “Relativistic hartree-slater values for K and L X-ray emission rates,” *At. Data Nucl. Data Tables*, vol. 14, no. 2, pp. 121–137, Aug. 1974.

[23] M. G. Pia *et al.*, “Evaluation of atomic electron binding energies for Monte Carlo particle transport,” *IEEE Trans. Nucl. Sci.*, vol. 58, no. 6, pp. 3246–3268, 2011.

[24] R. D. Deslattes, E. G. Kassler, P. Indelicato, L. De Billy, E. Lindroth, and J. Anton, “X-ray transition energies: New approach to a comprehensive evaluation,” *Rev. Mod. Phys.*, vol. 75, no. 1, pp. 35–99, 2003.

[25] W. Brandt and G. Lapicki, “Energy-loss effect in inner-shell Coulomb ionization by heavy charged particles,” *Phys. Rev. A*, vol. 23, no. 4, pp. 1717–1729, 1981.

[26] H. R. Verma, *Atomic and nuclear analytical methods*. Springer, 2007.

[27] Z. Pastuovic *et al.*, “SIRIUS - A new 6 MV accelerator system for IBA and AMS at ANSTO,” *Nucl. Instruments Methods Phys. Res. Sect. B Beam Interact. with Mater. Atoms*, vol. 371, pp. 142–147, 2016.